ACS APPLIED NANO MATERIALS

www.acsanm.org Article

Comparison of Copper(II) Oxide Nanostructures with Different Morphologies for Nonenzymatic Glucose Sensing

Baoyue Fan,[†] Brian D. Spindler,[†] Wenyang Zhao, Hoffman Chan, Zhao Wang, Minog Kim, Yevedzo Chipangura, Philippe Bühlmann, and Andreas Stein*

Cite This: *ACS Appl. Nano Mater.* 2023, 6, 1475−1486 Read Online

ACCESS | Metrics & More | Article Recommendations | Supporting Information

ABSTRACT: The glucose sensitivity achieved with copper(II) oxide particles with three different morphologies (spheres, platelets, and needles) for application in nonenzymatic glucose sensors was investigated. The morphologies of CuO nanoparticles were controlled by different synthesis parameters, including changes in precipitators of Cu(II) ions, pH values, calcination protocol, and the addition of surfactant and hydrogen peroxide. The role of copper(II) oxide particle morphology in nonenzymatic glucose sensing was studied. The primary driving factor in the electrocatalytic process was investigated for several morphological properties of the material. We studied the effects of exposed crystal faces, specific surface area, pore volume, and grain size of copper oxides on glucose sensitivity. This study showed that the electrocatalytic performance in glucose sensing correlates primarily with the grain size of copper oxide nanoparticles and the capacitance introduced therefrom. The needle-shaped CuO nanoparticles presented the optimal morphology in this application, resulting in good sensitivity to glucose (2.05 $mA \cdot mM^{-1} \cdot cm^{-2}$), a linear range of 0.05−5 mM glucose, and the best long-term stability among these materials. This work provides insight into the potential use of CuO-based materials in biosensors and into the major contributing factors of metal oxide-based nanoparticles in sensing applications.

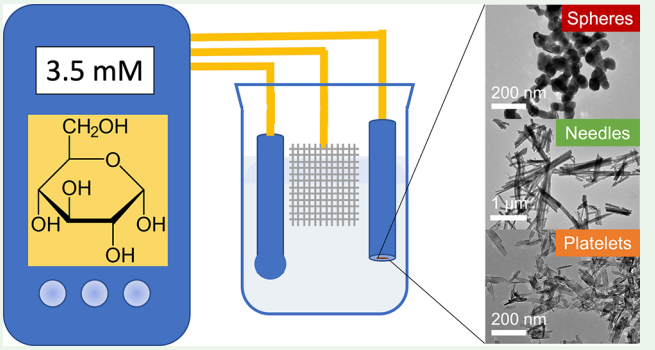

KEYWORDS: *nonenzymatic glucose sensing, electrocatalysis, copper oxide nanoparticles, morphology, grain size, surface area*

1. INTRODUCTION

Glucose sensors are designed to monitor blood glucose levels for tracking diabetes. Enzyme-based sensors have been widely used for glucose detection because of their excellent sensitivity and selectivity.[1] However, those sensors are limited by the nature of enzymes whose activity is highly sensitive to variations in temperature, pH value, oxygen concentration, etc. Therefore, researchers have also developed nonenzymatic sensors that overcome the instability problem of the enzymes.[2−5] Various nanostructured materials containing transition-metal centers have been studied in the context of electrochemical glucose sensing due to their ability to catalyze the oxidation of glucose;[2] these include noble metals such as Pt[6] and Au,[7] metal alloys,[8,9] and metal oxides such as zinc oxide (ZnO),[10] nickel oxide (NiO),[11] copper oxide (CuO, Cu_2O),[12,13] cobalt oxide (Co_3O_4),[14] titanium oxide (TiO_2),[15] and others. The application of many of these metals and metal alloys in nonenzymatic glucose sensors is restricted by their high price and susceptibility to Cl^- ion poisoning.[13] Therefore, with a goal to develop economical and sensitive nonenzymatic glucose sensors,[16] metal oxides have recently attracted more attention in this area.[17,18]

Copper(II) oxide (CuO) is a low-cost material and a p-type semiconductor with a band gap of 1.2 eV.[19] It has been investigated in a wide range of fields as a material for batteries,[20] sensors,[21] catalysts,[22] supercapacitors,[23] and adsorbents.[24] CuO has also been demonstrated to act as an electrocatalyst for nonenzymatic biosensing based on glucose oxidation.[12,25,26] In alkaline media, CuO is electrochemically oxidized to Cu(III) species, followed by a catalytic reaction in which glucose is oxidized to gluconic acid in the presence of the Cu(III) species, which are reduced to form CuO again. During this process, an electrical current is generated when electrons are exchanged between the CuO electrode and the glucose system. Consequently, the CuO-based sensor can serve as an amperometric sensor measuring the electric current changes as a function of glucose concentration.

Received: December 19, 2022
Accepted: December 27, 2022
Published: January 12, 2023

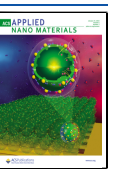

Scheme 1. Synthesis Conditions for CuO Nanoparticles with Different Morphologies, the Geometric Models (Spherical, Cylindrical, and Cuboid Models) Used to Simulate These Morphologies, and Application of the Nanoparticles in a Glucose Sensor

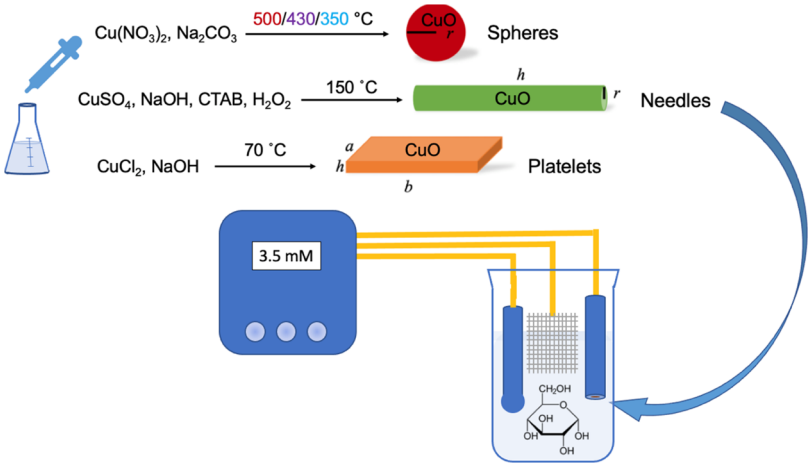

In previous studies, it was concluded that good electrocatalytic performance is possibly related to the surface area[27] of the material and/or its hierarchical structure.[28,29] CuO is a good candidate to study how particle morphology influences glucose sensing performance. Different shapes of CuO nanoparticles can be obtained by tuning the synthesis parameters. For example, Sun et al. prepared CuO nanoribbons by one-step water/ethanol hydrolysis of $Cu_3(OH)_4(SO_4)$.[30] Chen et al. synthesized CuO nanoclusters in a solvothermal route with the addition of polyvinylpyrrolidone.[31] Huang and co-workers reported that controlling the thermolysis of copper hydroxide can alter the final CuO morphology to produce either nanoplatelets or nanorods.[32] CuO microspheres were obtained in a template-assisted hydrothermal synthesis by Saraf et al.[33] A few publications reported that specific morphologies of CuO improved glucose sensitivities.[28,34,35] The glucose sensing performance was also related to specific crystal faces of CuO.[36,37] However, to date, studies on CuO-based materials in nonenzymatic glucose sensing still lack a more systematic investigation of the role of CuO particle morphology and an understanding of which specific factors contribute predominantly to the electrocatalytic performance.

In this study, we synthesized CuO nanoparticles with three different morphologies: spheres of various sizes, platelets, and needles (Scheme 1). We investigated how the synthesis influenced CuO morphologies and measured the glucose sensing performance of each material. Several factors were chosen to determine the primary contributors to the glucose sensing process, including the exposure of certain crystal faces, specific surface area, pore texture, and grain size of the copper oxides. We observed the strongest correlation between the grain size of copper oxide and the electrocatalytic performance for glucose sensing. CuO nanoparticles with needle morphology were optimal for this sensing application, as they provided both high glucose sensitivity and stability relative to the other nanoparticle morphologies examined here.

2. EXPERIMENTAL SECTION

2.1. Materials. All chemicals were used as received without further purification: copper(II) chloride dihydrate (crystalline certified), hydrogen peroxide (certified ACS, 30%), acetone (certified ACS) from Fisher Scientific; copper(II) nitrate trihydrate (ACS grade), cetyltrimethylammonium bromide (CTAB), α-D-glucose (ACS grade), Nafion perfluorinated ion-exchange resin (5 wt % solution in lower aliphatic alcohols/H_2O mix, contains 15−20% water) from Sigma-Aldrich; copper(II) sulfate pentahydrate (fine crystal, ACS grade) from Mallinckrodt; sodium hydroxide pellets (ACS grade) from Avantor Performance Materials; sodium carbonate anhydrous powder (ACS grade) from J.T. Baker; ethanol (anhydrous, 200 proof) from Pharmco-AAPER. Deionized (DI) water produced on-site using a Milli-Q PLUS reagent-grade water system to a minimum resistivity of 18.2 MΩ·cm was used in all experiments.

2.2.1. Synthesis of CuO Spheres (CuO-s). The -s suffix denotes spherical CuO particles. A volume of 40 mL of 0.1 M Na_2CO_3 solution was added dropwise to 40 mL of 0.1 M $Cu(NO_3)_2$ solution. A blue precipitate formed gradually during this process. After all of the Na_2CO_3 solution had been added, the mixture reached a pH of ∼10. The blue dispersion was maintained at room temperature for 30 min with magnetic stirring at a rate of 700 rpm. The $Cu_2(OH)_2CO_3$ product was separated by centrifugation at 11,000 rpm for 10 min, washed with DI water and then acetone, and dried at 110 °C overnight. Different grain sizes of CuO-s were obtained by calcining $Cu_2(OH)_2CO_3$ under various conditions. $Cu_2(OH)_2CO_3$ was calcined in static air in a tube furnace at 500 °C for 1 h, 430 °C for 0 min (i.e., no dwell time after the heating ramp), or 350 °C for 3 min (heating ramp rate 10 °C/min) to obtain samples CuO-s@500, CuO-s@430, CuO-s@350, respectively.

2.2.2. Synthesis of CuO Platelets (CuO-p). The -p suffix denotes CuO particles with platelet-like shape. CuO-p was synthesized by the following procedure. A mass of 170 mg of $CuCl_2{\cdot}2H_2O$ was dissolved in 200 mL of DI water to prepare a 5 mM $CuCl_2$ solution. After the solution was heated to 70 °C, 4 mL of an aqueous 0.75 M NaOH solution was added while stirring, resulting in a pH between 10 and 11 for the reaction mixture. The resulting brown dispersion was maintained at 70 °C for 1.5 h with magnetic stirring at a rate of 600 rpm. The product was separated by centrifugation at 8000 rpm for 10 min and washed with DI water and ethanol. The product was dried at room temperature.

2.2.3. Synthesis of CuO Needles (CuO-n). The -n suffix denotes needle-shaped CuO particles. CuO-n was synthesized following a published procedure.[38] First, 97.5 mL of an aqueous solution containing 1 mmol of $CuSO_4{\cdot}5H_2O$ and 0.5 mmol of CTAB was prepared in a 500 mL round-bottom flask. Then, 2.5 mL of 30% H_2O_2 was added dropwise. The mixed solution was sonicated for 20 min in a sonication bath. The pH was measured to be between 4 and 5. Then, 40 mL of 0.5 M NaOH was added dropwise and very slowly to avoid excessive foam formation in the flask. During this process, a brown precipitate formed, and bubbles were generated. The final pH was close to 14. The dispersion was stirred at a rate of 700 rpm for 2

https://doi.org/10.1021/acsanm.2c05433
ACS Appl. Nano Mater. 2023, 6, 1475−1486

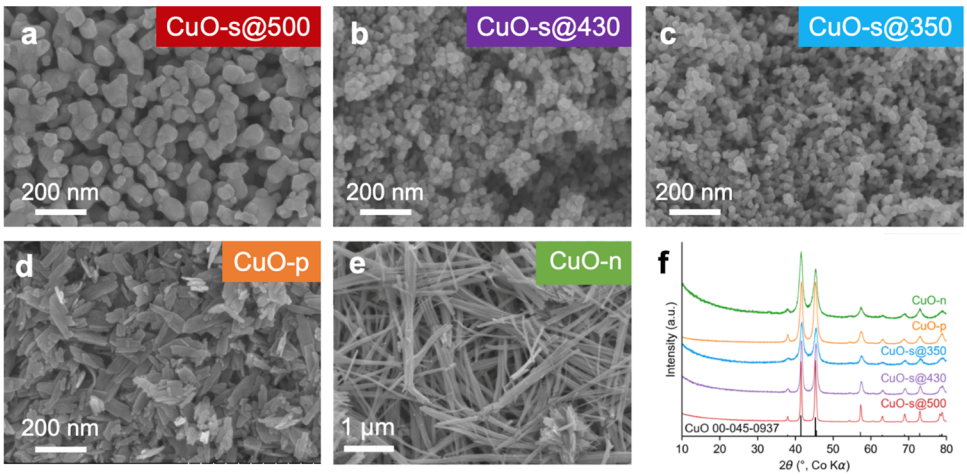

Figure 1. (a–e) SEM images and (f) XRD patterns of CuO nanoparticles with different morphologies.

h. The brown dispersion turned green after 30 min and then turned blue after 1.5 h. The precipitate was separated by centrifugation at 5000 rpm for 5 min and washed with DI water. The centrifugation/washing procedure was repeated five to six times until the pH value of the supernatant turned neutral. Then, the precipitate was calcined in static air in a tube furnace at 150 °C for 5 h with a heating ramp rate of 5 °C/min, producing CuO-n.

2.3. Fabrication of CuO-Modified Glassy Carbon Electrodes. Glassy carbon electrodes (GCE, 3 mm diameter) were polished over polishing cloths, first with 0.3 μm and then with 0.05 μm alumina slurry and thoroughly rinsed with water. Then, the electrodes were cleaned by ultrasonication in water and ethanol for a few minutes, and dried at room temperature for later use. A mass of 1.0 mg of CuO was dispersed in 1 mL of a 50:50 (v/v) ethanol/water mixture and was sonicated for 10 min. Then, 10 μL of a 5 wt % Nafion solution was added to the CuO dispersion, which was sonicated for 30 min. Next, 20 μL of the CuO/Nafion dispersion was dropped onto the surface of a pre-treated GCE and dried at room temperature before carrying out electrochemical experiments.

2.4. Characterization. Powder X-ray diffraction patterns were collected using an X'Pert Pro diffractometer with a Co Kα radiation source (λ = 1.789 Å) operating at 45 kV and 40 mA. Grain sizes were calculated using the Scherrer equation. Scanning electron microscopy images were obtained on a JEOL-6500F field emission gun-scanning electron microscope using a 5.0 kV accelerating voltage. Prior to SEM imaging, all samples were coated with a 50 Å Pt film. Transmission electron microscopy (TEM) images were acquired on an FEI Tecnai T12 microscope operating at 120 kV accelerating voltage. The TEM samples were prepared by dispersing the nanoparticles in ethanol and bath-sonicating them for about 15 min. Formvar-coated Cu grids were dipped into the suspension and dried. FTIR spectra were obtained with a Nicolet Magna 760 IR spectrometer using KBr pellets. N_2 sorption measurements were carried out on a Quantachrome Autosorb iQ2 analyzer. All samples were degassed at 120 °C for 16 h prior to the analysis. Brunauer–Emmett–Teller surface areas were evaluated from the linear region (0.05–0.35) of the adsorption isotherms. The total pore volumes were obtained from the last adsorption data point in the isotherms. X-ray photoelectron spectroscopy (XPS) spectra were collected with a PHI 5000 VersaProbe III Photoelectron Spectrometer with an Al Kα source ($h\nu$ = 1486.6 eV), an accelerating voltage of 15 kV, and a beam power of 50 W. High-resolution spectra were collected using a pass energy of 55.0 eV. During XPS measurements, the sample was neutralized to prevent charge buildup and distortion of the spectra. Binding energies for all spectra were referenced to the primary C_{1s} peak corresponding to the C–C binding energy (284.8 eV).

2.5. Electrochemical Measurements. Electrochemical experiments were carried out on a CHI-660C (from CH Instruments) electrochemical workstation with a three-electrode system at room temperature. A CuO-modified GCE was used as the working electrode, a Ag/AgCl (3 M KCl) electrode with a porous glass junction served as the reference electrode, and a platinum mesh acted as the counter electrode. The electrolyte was 10 mL of 0.1 M NaOH aqueous solution for all experiments. Cyclic voltammetry (CV) was performed at a scan rate of 50 mV/s. Amperometric responses were collected using the i–t (current–time) mode at a specific voltage by successive additions of 0.1 M glucose solution into 10 mL of 0.1 M NaOH electrolyte under stirring. The voltage was chosen to correspond to the glucose oxidation peak in the CV curves.

2.6. Electrochemical Impedance Spectroscopy (EIS). EIS spectra were collected using a 3-electrode cell with a Pt mesh counter electrode and a Ag/AgCl double-junction reference electrode in 0.1 M NaOH solution or in 0.1 M NaOH/5 mM glucose solution. The spectra were obtained with a Solartron SI1287 electrochemical interface with a SI1255B frequency response analyzer and applying a sinusoidal perturbation with a 10 mV amplitude from 1 MHz to 100 mHz. Ten points per decade frequency were collected. The impedance spectra were collected at the open circuit potential in each solution and at potentials of 0.55 and 0.6 V vs Ag/AgCl. For impedance spectra at potentials other than the open circuit potential, the electrode was held at 0.55 or 0.6 V for 120 s immediately prior to the impedance measurement to ensure that the current at the working electrode reached a steady state for impedance analysis. The impedance spectra were fitted using ZView software from Scribner Associates. To avoid fitting artifacts at high frequencies, fitting was performed in the range of 100 kHz to 100 mHz.

3. RESULTS AND DISCUSSION

3.1. Effect of Synthesis on Morphology of CuO Nanoparticles. Copper oxide nanoparticles with different morphologies were produced by different synthetic methods. To produce CuO spheres, sodium carbonate was used to precipitate Cu^{2+} ions from aqueous solution. The optimal concentration for both carbonate and Cu^{2+} ions was found to be 0.1 M to obtain relatively uniform spheres. The XRD pattern in Figure S1a shows that the intermediates obtained from 0.1 M and 0.3 M Cu^{2+} and CO_3^{2-} were amorphous and crystalline $Cu_2(OH)_2CO_3$, respectively. However, SEM images in Figure S1b and Figure S1c show that the low concentration (0.1 M) helped to form well-dispersed spheres, whereas the higher concentration (0.3 M) did not provide the targeted spherical morphology. To synthesize spherical CuO particles with different sizes, the intermediate amorphous $Cu_2(OH)_2CO_3$ (Figure S1) was calcined at 500, 430, and 350 °C, respectively. SEM images (Figure 1a–c) show that the particle size decreases as the calcination temperature decreases,

https://doi.org/10.1021/acsanm.2c05433
ACS Appl. Nano Mater. 2023, 6, 1475–1486

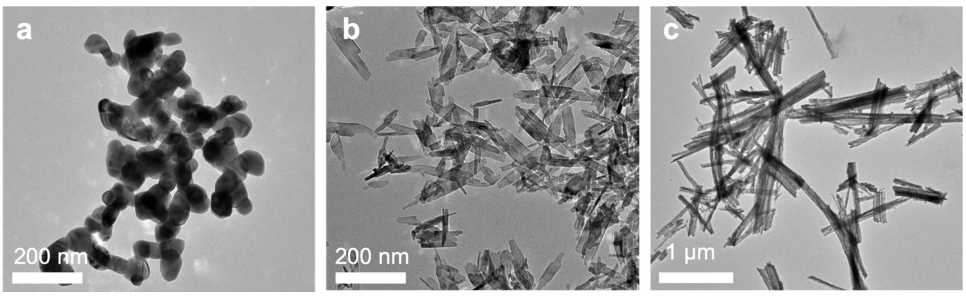

Figure 2. TEM images of CuO nanoparticles with different morphologies: (a) spheres from sample CuO-s@500, (b) platelets from sample CuO-p, (c) needles from sample CuO-n.

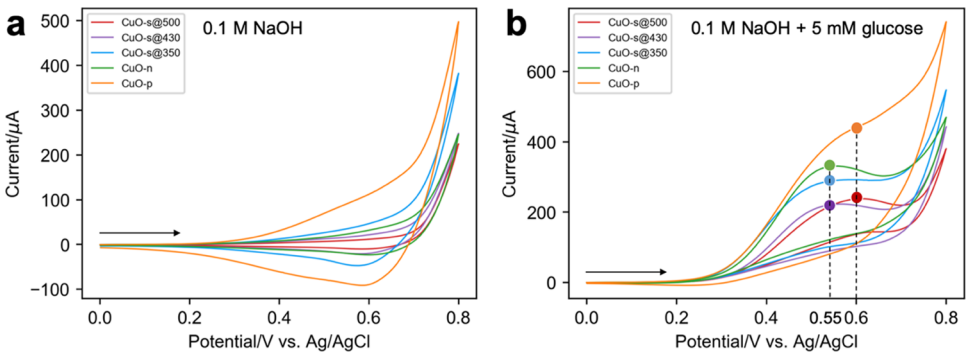

Figure 3. Cyclic voltammograms of the various CuO-modified electrodes in 0.1 M NaOH aqueous solution in the absence (a) or presence (b) of glucose at a scan rate of 50 mV/s.

the average diameters being 64 ± 6 nm for CuO-s@500, 33 ± 1 nm for CuO-s@430 and 28 ± 1 nm for CuO-s@350 (Figure S2). All powder XRD patterns of the nanoparticles (Figure 1f) matched the reflections of CuO (PDF# 00-045-0937) and indicated that this phase was highly crystalline. However, the distinct differences in XRD peak widths observed for each sample indicated that the CuO nanoparticles have different grain sizes. Using the Scherrer equation, the average grain sizes of spherical particles were estimated to be 61 ± 4 nm (CuO-s@500), 36 ± 3 nm (CuO-s@430), and 26 ± 4 nm (CuO-s@350). The close agreement between the grain sizes calculated from XRD patterns and particle sizes measured from SEM images implies that most particles consist of a single-grain CuO sphere.

CuO nanoplatelets were synthesized by precipitating Cu^{2+} with OH^- at 70 °C from aqueous solution. SEM images (Figure 1d) and TEM images (Figure 2b) show the platelet-like features in this sample, and the average grain size of the particles is estimated to be 27 ± 1 nm from the XRD pattern. Nevertheless, due to the platelet-like shape, it is hard to identify a single grain from a platelet. The crystal growth of this sample will be discussed in detail in Section 3.3.1.

Needle-like CuO particles were acquired following a published procedure. Pandey et al. observed that a needle-like morphology is obtained when Cu^{2+} is precipitated out by hydroxide ions in the presence of the surfactant CTAB and H_2O_2.[38] To better understand the role of each component in this procedure, we carried out control experiments in which either H_2O_2 or CTAB was left out from the reaction mixture. The following equilibria contribute to the formation of CuO when NaOH is used to precipitate Cu^{2+} ions in a solution at pH 14[39]

$$Cu^{2+}_{(aq)} + 2OH^-_{(aq)} \leftrightharpoons Cu(OH)_{2\,(s)} \quad (1)$$

$$Cu(OH)_{2\,(s)} + 2OH^-_{(aq)} \leftrightharpoons Cu(OH)_4{}^{2-}{}_{(aq)} \quad (2)$$

$$Cu(OH)_4{}^{2-}{}_{(aq)} \leftrightharpoons CuO_{(s)} + H_2O + 2OH^-_{(aq)} \quad (3)$$

We observed that when the reaction mixture lacks H_2O_2, a blue precipitate forms first, which is likely to be $Cu(OH)_2$, whereas for the original reaction mixture with H_2O_2, brown CuO precipitates out first. From this observation, we propose that the presence of H_2O_2 promotes the nucleation of CuO crystals by providing fewer oxygen vacancies in the CuO structure so that the intermediate $Cu(OH)_2$ is used up too quickly to be observed. Furthermore, products synthesized without H_2O_2 had larger grains than materials made with both H_2O_2 and CTAB (35 vs 23 nm), and large platelets were observed in the SEM image (Figure S3b) instead of the targeted needle-like morphology. We conclude that the addition of H_2O_2 is a key factor to produce the needle-like morphology of CuO.

The sample obtained without adding CTAB had a grain size of 22 nm, similar to that of the targeted needle-like CuO particles. However, as seen in its SEM image (Figure S3c), the needles were thicker (compared with Figure 1e). This implies that CTAB may hinder the aggregation of particles by keeping them apart from one another to produce thinner needles. At the end of the synthesis with CTAB, after the washing and calcination steps, CTAB is no longer present in the CuO-n particles, as confirmed by the absence of C−H stretching peaks in the FT-IR spectrum of CuO-n (Figure S4).

3.2. Glucose Sensing Performance of CuO Nanoparticles. The nonenzymatic glucose sensing performance with various CuO-modified glassy carbon electrodes was investigated. This section will discuss the electrocatalytic behavior of CuO in glucose sensing and the sensitivity of the CuO particles with different morphologies as determined by cyclic voltammetry (CV) and amperometry.

https://doi.org/10.1021/acsanm.2c05433
ACS Appl. Nano Mater. 2023, 6, 1475−1486

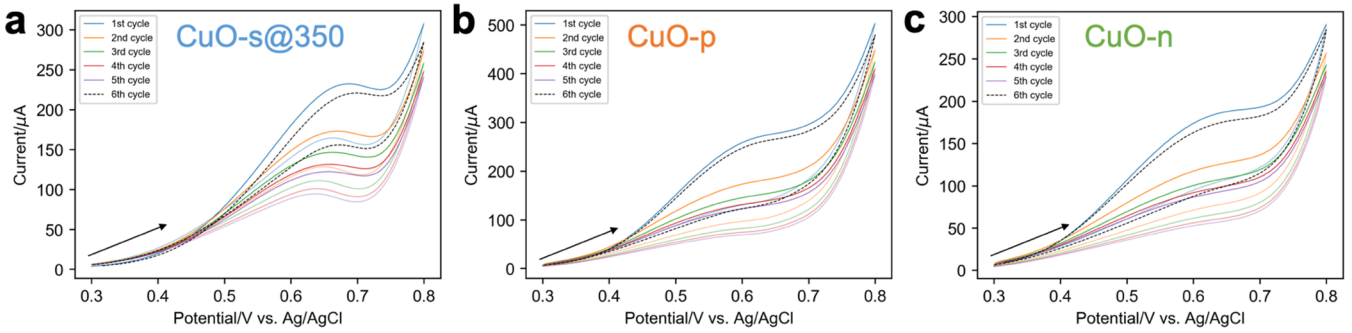

Figure 4. Cyclic voltammograms of the CuO-modified electrodes in 0.1 M NaOH aqueous solution with 5 mM glucose at a scan rate of 50 mV/s: (a) CuO-s@350, (b) CuO-p, and (c) CuO-n. Five cycles (1st−5th cycle) were collected continuously, then after waiting for 5 min, the 6th cycle was collected.

3.2.1. Electrocatalytic Behavior of CuO in Glucose Sensing. To study the sensing mechanism of the CuO-modified electrodes toward glucose, CV measurements were carried out in 0.1 M NaOH aqueous solution in the absence or presence of glucose at a scan rate of 50 mV/s. As shown in Figure 3a, all of the electrodes showed a relatively low current intensity in the solution without glucose. In contrast, peaks were observed in the CV with 5 mM glucose (Figure 3b). Specifically, for the differently sized CuO nanospheres a peak occurred at different potentials, as indicated by the dots in Figure 4b. The largest CuO spheres (grain size: 61 nm) showed a peak at 0.6 V, whereas the peaks for the other two spherical CuO materials (grain sizes: 36, 26 nm) were at 0.55 V. This could be explained by the smaller grain size of CuO spheres facilitating the glucose oxidation at a relatively low potential. Size-dependent electrode potentials have also been reported for other types of nanoparticles.[40] The peaks for needle-like CuO-n and CuO-p nanoplatelets occurred at 0.55 and 0.60 V, respectively.

Previous research has demonstrated the capability of CuO-based electrodes to function as electrocatalytic glucose sensors. Mechanistic studies of CuO in the glucose sensing process have proposed the involvement of Cu(III) species generated on the electrode surface at around 0.6 V vs Ag/AgCl,[41] which further oxidizes glucose, yet there is only limited evidence for the Cu(III) species. The presumed mechanism includes two net reaction steps

$$CuO + OH^- \rightarrow CuOOH + e^- \quad (4)$$

$$2\,CuOOH + C_6H_{12}O_6(\text{glucose}) \rightarrow 2\,CuO + C_6H_{10}O_6(\text{gluconolactone}) + 2\,H_2O \quad (5)$$

During the first electron transfer step (reaction 4), a Cu(II) ion at the surface of CuO loses an electron to give a Cu(III) species, a process made possible by the high hydroxide concentration. The unstable CuOOH quickly oxidizes glucose to the gluconolactone (reaction 5). Considering that the potential in the electron transfer step should not be affected by the glucose, a peak arising from the Cu(II)/Cu(III) redox couple is expected to be observed even in the absence of glucose. However, the cyclic voltammograms of the various CuO-modified electrodes in 0.1 M NaOH aqueous solution without glucose (Figure 3a) do not show any peak for the Cu(II)/Cu(III) redox couple at the potentials where peaks are observed in Figure 3b. The disappearance of the redox peak has been attributed to the passivation of Cu(II) on the surface.[42,43] Previous research by Prabhu et al. revealed an oxidative wave for the Cu(II)/Cu(III) redox couple in the initial CV scan using a Cu(II)-ion modified GCE, and this wave disappeared in the following scans due to rapid Cu_2O_3 film formation and a passivation process.[42,44,45] In our case, a Cu(II)/Cu(III) peak is not observed at all in the blank NaOH solution because our electrodes are coated with copper(II) oxide, not free cupric ion. However, the passivation process is inhibited by the incorporation of glucose in the NaOH solution.[44] Once glucose is added in the electrolyte, the initial electron transfer step that forms CuO from CuOOH (reaction 4) is coupled to a chemical reaction that removes the product of this electron transfer reaction and chemically regenerates the reactant (reaction 5). The reductive scan of the CV in the presence of glucose provides evidence for the mechanism proposed above. As seen from Figure 3b, the currents of both the forward and backward scans in the CV stay positive, without reversal of electron flow.[46] The chemical reaction (reaction 5) between CuOOH and glucose produces CuO, which results in CuO being continuously regenerated. In this case, CuO serves as an electrocatalyst in the glucose oxidation process. Although only a small fraction of active CuO exists on the surface, it can promote the glucose oxidation and keep generating the current in the glucose sensing process.

Furthermore, to study the chemical stability of the CuO nanoparticles on the working electrode, successive CV cycles were performed. The CV curves depicted in Figure 4 show six cycles for three CuO-modified electrodes (CuO-s@350, CuO-p, and CuO-n). These three CuO materials were chosen because they have similar average grain sizes (26, 23, 27 nm) with various morphologies. First, cycles 1−5 were collected consecutively. There is significant attenuation between the first and second cycles. Because the peak potentials for these cycles are close to each other and indeed the peak position is consistent with a slightly less kinetically limited reaction, it does appear that this rather large current decrease may be related to limitations of the nonlinear diffusion within the oxide film. For all of the materials measured, the current intensity continued to decrease after each cycle. We considered two possible reasons for this behavior: (1) the number of active sites of CuO may be reduced during cycling or (2) the diffusion of glucose from the bulk solution to the electrode surface may not be sufficiently fast at the scanning rates used. To test this, after the five consecutive cycles, the solution containing the electrode was left for 5 min without stirring and then the sixth cycle (dotted line in Figure 4) was collected. The curve in the sixth cycle turned back to nearly the same position as in the 1st cycle. On this basis, we conclude that the

https://doi.org/10.1021/acsanm.2c05433
ACS Appl. Nano Mater. 2023, 6, 1475−1486

number of active sites of CuO is not diminished in the CV cycles; instead, as the glucose near the electrode is used up in the past cycle, the glucose from the bulk solution may be slow to diffuse to the electrode surface, leading to a decrease in current for the continuous scans. The 5 min interval provided more time for the diffusion of glucose so that the intensity was restored. Further evidence for this mass transfer limitation comes from the observation that when five continuous CV scans were performed in 0.1 M NaOH aqueous solution with a high concentration of glucose (37.5 mM), the current did not decrease significantly (Figure S5). Also, the oxidation state of Cu(II) did not change after measurements as determined by XPS analysis (Figure S7). Therefore, we conclude that the CuO nanoparticles were stable in the short-term experiment, given that the same catalytic activity to glucose was maintained. However, in longer-term studies, the sensitivity to glucose decreased over a period of days (Figure S8 and Table S1). Among these samples, it was maintained best for CuO-n (decrease of 11% after 5 days, 16% after 10 days). Notably, the sample morphology did not change after 10 days, at which time the sensors had been used multiple times (Figure S11).

3.2.2. Sensitivity of CuO Nanoparticles with Different Morphologies for Glucose Sensing. The glucose sensing performance of the CuO materials was evaluated by the amperometric response of each CuO-modified electrode. A bare glassy carbon electrode was also tested for comparison (Figure S12). In the amperometry experiments, given aliquots of 0.1 M glucose were added to 10 mL of 0.1 M NaOH with continuous stirring of the solution during the measurement. The stirring was intended to avoid a concentration gradient from the bulk solution to the electrode surface during the addition of glucose. Figure S12 shows no significant current change for the bare GCE during the whole measurement, whereas the current increased with glucose concentration for the CuO-modified electrode. Calibration plots derived from the amperometric response are shown in Figure 5. While there was some electrode-to-electrode variation (likely due to inhomogeneities in the CuO−Nafion films, see Figure S11), for all CuO-modified electrodes, the current intensity increased linearly with the addition of glucose in the concentration range from 0.05 to 1 mM (correlation coefficient > 0.999 for all measurements). The normal fasting blood glucose concentration for an adult human is between 3.5 and 5.5 mM.[47] Figure S13 summarizes the calibration plots of all electrodes in the concentration range from 0.05 to 5 mM. The linear range of electrodes modified with CuO-n and CuO-p particles extended to 5 mM with a correlation coefficient > 0.99, whereas the use of the CuO-s particles resulted in a less linear behavior above 1 mM. Therefore, to compare the sensitivities of the materials in this work, we use as the sensitivities the calibration slopes obtained in the 0.05−1 mM range. They are summarized in Table 1 and are compared with the sensitivities for other reported nonenzymatic glucose sensors in Table S2. CuO-n, CuO-p, CuO-s@350, and CuO-s@430 modified electrodes showed good sensitivities to glucose between 1.90 and 2.09 $mA{\cdot}mM^{-1}{\cdot}cm^{-2}$; however, CuO-s@500 displayed a sensitivity of only 1.52 $mA{\cdot}mM^{-1}{\cdot}cm^{-2}$. In the next section, we will discuss possible factors that may contribute to the difference in the sensitivities for these five materials.

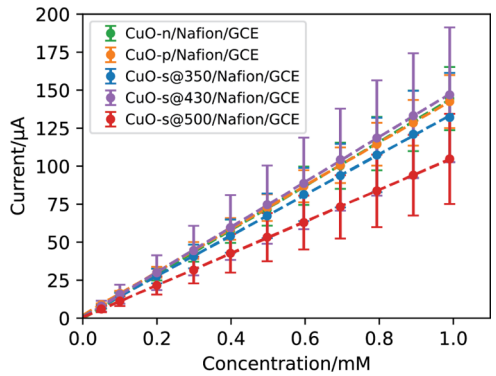

Figure 5. Comparison of calibration curves of the five CuO/Nafion/GCE electrodes derived from the amperometric response with successive additions of glucose into 0.1 M NaOH at a specific potential. The voltage was chosen as the glucose oxidation peak in their corresponding CV curves (+0.55 V vs Ag/AgCl for CuO-s@430, CuO-s@350, and CuO-n, +0.60 V vs Ag/AgCl for CuO-s@500 and CuO-p). Each type of electrode was tested in quadruplicate. The relative errors of the slopes determined from the error bars in current are between 10 and 30%. Note that the line for CuO-n (green) overlaps with the lines for CuO-p (orange) and CuO-s@350 (blue). All raw data are shown in Figure S13.

3.3. Correlation between Morphologies of CuO Nanoparticles and Their Glucose Sensing Performance.

Numerous researchers have demonstrated that various factors affect the sensing performance of metal oxides. A common view is that materials with high specific surface area promote electrochemical sensing performance.[27] Katoch et al. also studied how grain size and crystallinity of the material influence gas sensing performance.[48] In addition, a computational study showed that different crystal facets in CuO might contribute to the glucose sensing performance.[37] Here, we used the CuO nanoparticles with different morphologies to test possible hypotheses including that the crystal faces (Section 3.3.1), specific surface area (Section 3.3.2), grain size (Section 3.3.3), and electronic properties (Section 3.3.4) of CuO nanoparticles influence their sensitivity to glucose when used in amperometric sensing.

3.3.1. Influence of Crystal Faces of CuO Nanoparticles on Glucose Sensing. The morphology of a crystalline material affects which crystal facets are predominant on the particle surface. To study the crystal formation of the nanoparticles with different morphologies, selected-area electron diffraction (SAED) experiments were performed. The TEM image in Figure 6a shows an aggregate of multiple CuO-s@500 spheres, and the SAED pattern in Figure 6b provides evidence for the polycrystalline nature of the aggregate sample in this area, with a series of diffraction rings indicating that there are many grains in this area at various rotations around the center beam, with no preferred orientation. A single particle of CuO-s@500 was captured in Figure S14, and the spot diffraction pattern agrees with our previous observation that the spherical particles consist of single grains. For the platelet sample, a single platelet was chosen (Figure 6c), and its corresponding SAED pattern (Figure 6d) indicated that the platelet grew along the [010] and [100] directions. Moreover, for the CuO needles, the TEM image in Figure 6e shows that each needle is composed of a large number of small grains, their average size being 11 ± 1 nm (Figure S15). The grain sizes measured from the TEM images are smaller than the value (23 ± 3 nm) estimated from XRD patterns because large grains have a greater contribution to the peak intensity in XRD patterns; however, those large grains were not easily captured in the

https://doi.org/10.1021/acsanm.2c05433
ACS Appl. Nano Mater. 2023, 6, 1475−1486

Table 1. Calibration Slopes, Sensitivities, Grain Sizes, Particle Sizes, and Pore Texture of the CuO Nanoparticles with Different Morphologies

sample	CuO-s@500	CuO-s@430	CuO-s@350	CuO-p	CuO-n
calibration slope ($\mu A \cdot mM^{-1}$)	108 ± 33	148 ± 44	134 ± 33	143 ± 13	145 ± 22
sensitivity ($mA \cdot mM^{-1} \cdot cm^{-2}$)[a]	1.52 ± 0.46	2.09 ± 0.62	1.90 ± 0.46	2.02 ± 0.18	2.05 ± 0.31
grain size (nm)[b,d]	61 ± 4	36 ± 3	26 ± 4	27 ± 1	23 ± 3 (11 ± 1)[e]
particle size (nm)[c,d]	64 ± 6	33 ± 1	28 ± 1	(41 ± 7) × (143 ± 17)[f]	(61 ± 6) × (970 ± 88)[g]
BET specific surface area ($m^2 \cdot g^{-1}$)[d]	20 ± 2	35 ± 1	44 ± 0	54 ± 11	34 ± 12
total pore volume at p/p_0 = 0.99 ($cm^3 \cdot g^{-1}$)	0.42 ± 0.04	0.70 ± 0.01	0.92 ± 0	0.58 ± 0.04	0.22 ± 0.01
V_{micro} (SF method)[h] ($cm^3 \cdot g^{-1}$)	0.008 ± 0.001	0.015 ± 0	0.016 ± 0.007	0.019 ± 0.009	0.012 ± 0.008
V_{micro} (DR method)[h] ($cm^3 \cdot g^{-1}$)	0.006 ± 0.001	0.013 ± 0	0.016 ± 0.001	0.022± 0.003	0.013 ± 0.004
$V_{meso+macro}$ (BJH)[i] ($cm^3 \cdot g^{-1}$)	0.42 ± 0.03	0.69 ± 0.02	0.92 ± 0.01	0.58 ± 0	0.21 ± 0.01
micropore portion ($V_{micro,SF}/V_{total}$)	2%	2%	2%	3%	5%
average $S(110)/V$[j] (nm^{-1})	0.05	0.09	0.11	0.05	0.23

[a]Sensitivities are normalized to the geometric area of the glassy carbon electrode. [b]Grain sizes were estimated from XRD patterns. [c]Particle sizes were measured from scanning electron microscopy images (sphere sizes) and transmission electron microscopy images (sizes of needles and platelets). [d]The margins of error are reported as 95% confidence intervals. [e]Grain size in parenthesis estimated from TEM images. [f]The platelet dimensions were measured as $a \times b$ along the unit cell directions of the crystal structure from TEM images. The thickness (c direction) could not be determined from the TEM images. [g]Dimensions of needles are thickness × length. The needles are composed of small grains with diameters of 11 ± 1 nm. [h]Micropore volume (V_{micro}) was calculated by the Dubinin−Radushkevich (DR) method and the Saito−Foley (SF) method. [i]Mesopore and macropore volume ($V_{meso+macro}$) was calculated by the BJH (Barrett−Joyner−Halenda) method. The margins of error are reported at a confidence level of 95%. [j]Theoretical total areas of accessible (110) faces with respect to the volume ($S(110)/V$) in the crystal structure of CuO particles with different morphologies. The radii or lengths estimated from electron microscopy images in real samples were used for the dimensions. More details are provided in the Supporting Information.

TEM images. We also observed a preferred orientation in the SAED pattern of the needle-like sample (Figure 6f), judging from the fact that several spots were intense in the diffraction pattern even though this area contained a large number of small particles. The smaller particles are aggregated along the [001] direction to form long, micrometer-sized needles (Figure 6c).

On the basis of the different crystal morphologies, we propose three geometric models to represent each material, as shown in Scheme 1: a spherical model for nanospheres; a cylindrical model for needle-like particles, and a cuboid model for nanoplatelets. Khairy et al. investigated the binding energies between specific crystal facets and glucose molecules and concluded on the basis of density functional theory (DFT) calculations that facets with high concentrations of Cu and O atoms controlled the sensitivity to glucose.[37] They concluded that the (110) facets of CuO have the most negative binding energy with glucose. Thus, we hypothesize that the relative area of exposed (110) facets per unit volume correlates to the glucose sensing performance.

For each geometry, the total area of accessible (110) faces with respect to the volume $S(110)/V$ in the crystal structure was estimated (Tables 1 and S3) following the procedures described in the Supporting Information. For CuO spheres, the total accessible area of (110) faces increases with decreasing grain size, following the same trend as sensitivity values. However, for samples with different morphologies, comparing the $S(110)/V$ values with the glucose sensing results, there was no clear correlation between the crystal faces and sensing performance. For example, even though the CuO-p nanoplatelets have the smallest accessible (110) face-to-volume ratio, they exhibit high sensitivity to glucose as shown in Table 1. Therefore, the exposed (110) facets on the CuO surface do not appear to be the primary contributors to the glucose sensitivity for the nanoparticle morphologies studied here, and the hierarchical structures prepared by Khairy et al.[37] may be needed to see such an effect. We note, however, that the sample with the highest $S(110)/V$ value, CuO-n needles, displayed both high glucose sensitivity and high long-term stability in comparison to the other materials examined here.

3.3.2. Influence of Porosity and Specific Surface Area of CuO Nanoparticles on Glucose Sensing. The catalytic effect of a material may also be attributed to its specific surface area and porosity. Nitrogen sorption experiments were performed for all types of CuO samples. The nitrogen sorption isotherms shown in Figure 7 were all of Type II, with the knee point at a very low relative pressure and the unrestricted uptake value at a high pressure. The specific surface areas and pore structure data are summarized in Table 1. For the three CuO spherical samples, all of which consisted of single-grain nanoparticles, the specific BET surface areas followed the same trend as the theoretical specific surface areas in the spherical models (Figure S16). The experimentally determined specific BET areas are larger than the theoretical values, which may be due to textural pores in these samples (i.e., pores between spheres in aggregates). In all samples, the largest contributions to the total pore volume are from mesopores (2−50 nm) and macropores (>50 nm), whereas the micropore fraction (<2 nm) is calculated to be only 2−5% for these five materials, as shown in Table 1. Thus, glucose molecules should be able to diffuse in most pores of these CuO materials, considering that the kinetic diameter of glucose is estimated to be approximately 0.8 nm.[49] The four materials showing similarly high sensitivity to glucose (~2 $mA \cdot mM^{-1} \cdot cm^{-2}$), CuO-s@430, CuO-s@350, CuO-p, and CuO-n have significantly different total pore volumes, micropore fractions, or mesopore and macropore fractions. Therefore, porosity is not a limiting factor in the glucose sensing process for electrodes made with these materials.

In addition, the specific BET surface areas of the materials with different morphologies do not show a strong correlation with the glucose sensing process; for example, the specific BET surface areas of CuO-p and CuO-n differ by 37%, whereas their glucose sensitivities differ by less than 2%. This can be explained by dramatic differences between chemical environments of glucose sensing and nitrogen sorption. The specific

https://doi.org/10.1021/acsanm.2c05433
ACS Appl. Nano Mater. 2023, 6, 1475−1486

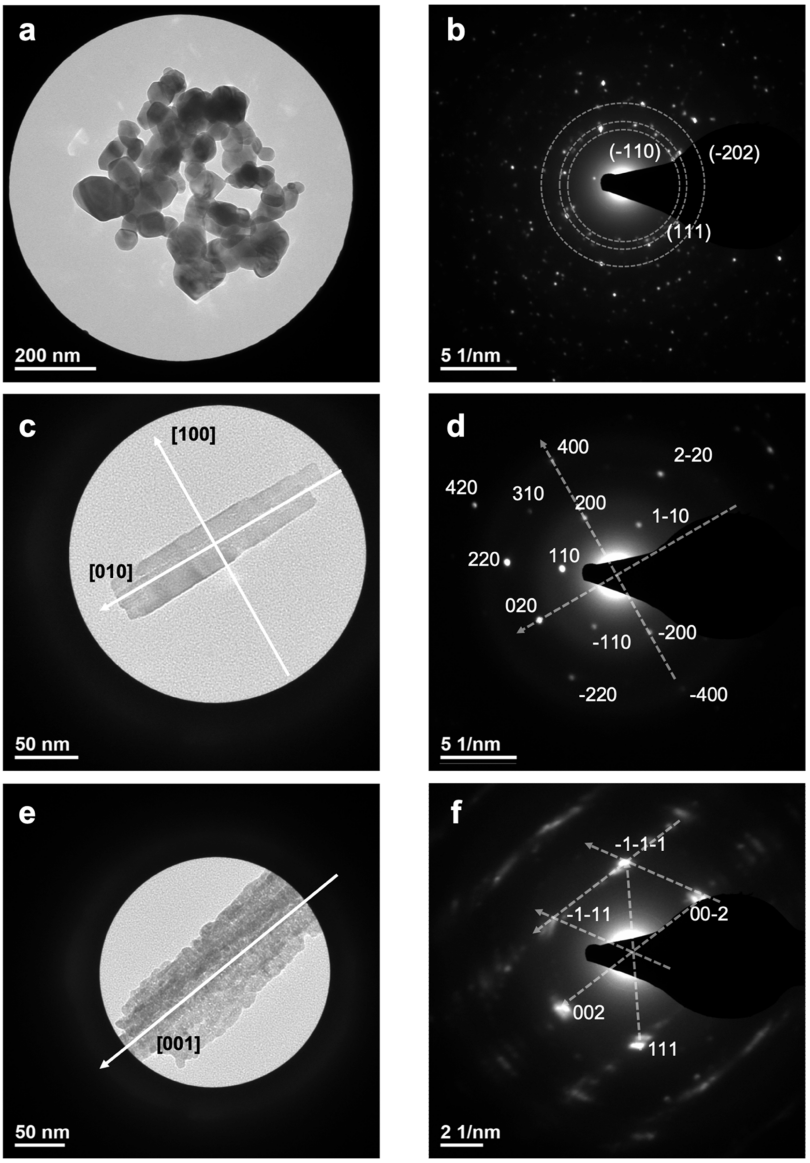

Figure 6. TEM images and the corresponding SAED patterns of the CuO nanoparticles with different morphologies: (a, b) CuO-s@500, (c, d) CuO-p, and (e, f) CuO-n. Reflections in (b, d, f) match those of CuO (PDF# 00-045-0937). Arrows in (c, e) show the crystal growth directions.

BET surface areas are calculated from the nitrogen sorption isotherms, which strictly describe how the pores in the dried and degassed sample are accessible to nitrogen molecules from the gas phase. However, the glucose sensing performance is evaluated for the CuO-modified electrodes in aqueous solution, with CuO particles embedded in a Nafion matrix. This difference makes the pore structure data obtained from nitrogen sorption measurements not directly applicable to the actual electrochemical set-up, especially considering that the surface of CuO becomes hydrolyzed in an alkaline medium. For the spherical CuO nanoparticles, however, the specific BET surface area is directly determined by the grain size (Figure S16) and thus correlated to the glucose sensitivity. Therefore, the BET surface area may still be a useful indicator for glucose sensing performance on materials with the same or similar morphology as long as the surface is electrochemically accessible. Consistent with these conclusions is the observation that a commercial CuO material with nearly spherical shape has a BET surface area of 14 $m^2 \cdot g^{-1}$ (Figure S19) and has relatively low sensitivity to glucose (1.44 $mA \cdot mM^{-1} \cdot cm^{-2}$, Figure S20).

3.3.3. Influence of Grain Size of CuO Nanoparticles on Glucose Sensing. Our study established a correlation between grain size of the CuO nanoparticles with the sensitivity to glucose. As shown in Table 1, one common factor shared among the CuO-s@350, CuO-n and CuO-p is the grain size. All of these three materials have a relatively small grain size between 20 and 30 nm, and their sensitivities toward glucose reach ~2 $mA \cdot mM^{-1} \cdot cm^{-2}$. The difference between the sensitivities of CuO-s@430 and CuO-s@350 is not statistically significant, which might be due to the similarity in their particle (grain) size distribution as shown in Figure S2b,c. As the grain size is further increased to a value of 61 nm, the sensitivity drops to 73% of the maximum. The grain size determined from powder XRD describes the average size of crystallites in a material, so it is also related to the specific surface area and the crystal structure of the material. For a material with specific morphology, a decrease in the size of exposed grains can increase the specific surface area of the material and increase

https://doi.org/10.1021/acsanm.2c05433
ACS Appl. Nano Mater. 2023, 6, 1475−1486

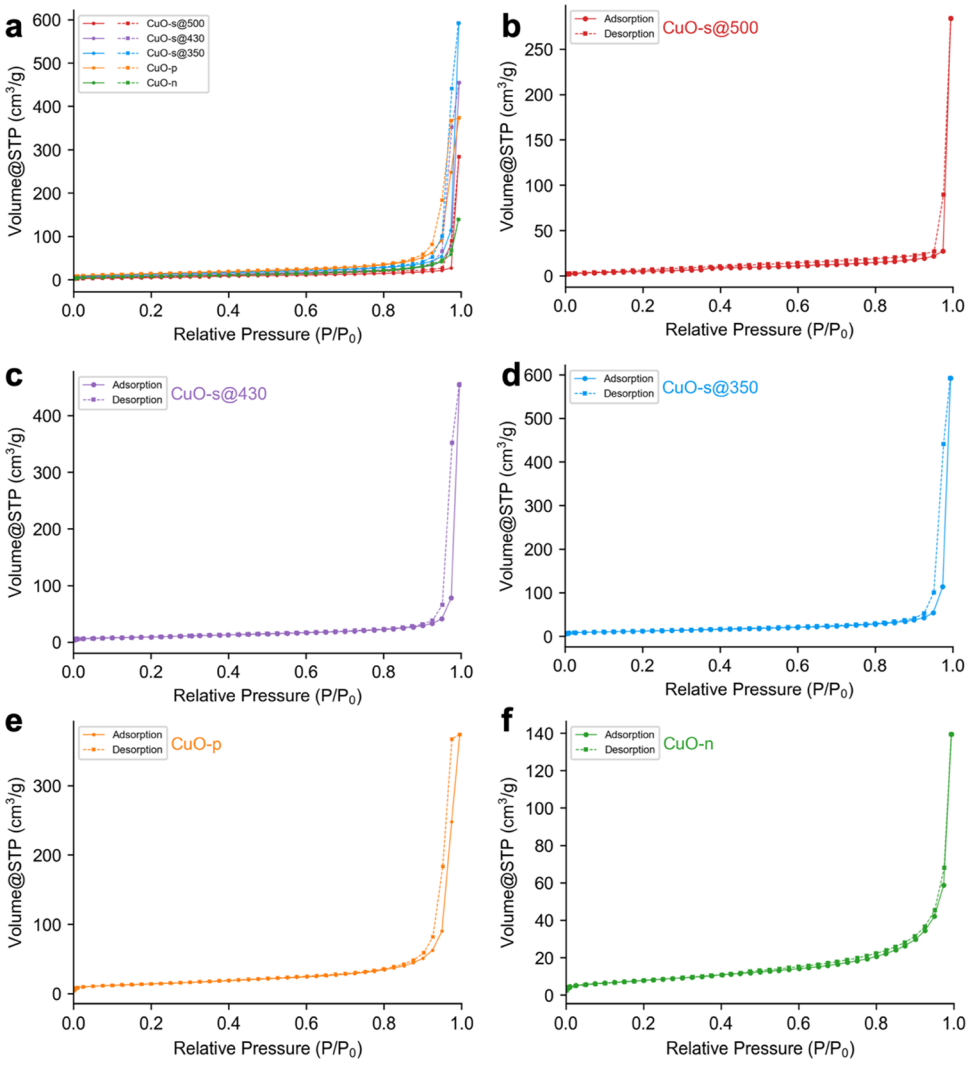

Figure 7. Nitrogen sorption isotherms of CuO nanoparticles with different morphologies. (a) Comparison of all materials, and individual isotherms for (b) CuO-s@500, (c) CuO-s@430, (d) CuO-s350 (e) CuO-p, and (f) CuO-n.

the number of active sites on its surface. In spherical CuO samples, each particle is a single grain. As the grain size decreases, the number of active sites increases, which promotes sensitivity. However, this does not apply to the polycrystalline platelet or needle-like CuO particles because each particle consists of many small grains, which gives fewer accessible active sites. A previous study on ZnO nanofibers used in a CO gas sensor also investigated the effect of grain size on its gas sensing performance.[48] The researchers stated that the small grains in that material may provide a large number of grain boundaries, leading to a high sensing response. This may also apply to the polycrystalline CuO nanoparticles in our study. Similar effects were also found in a ZnO−SnO_2 composite serving as a H_2-selective sensor.[50] Other researchers have studied metal oxide films and found that grain size is an essential parameter to control the response in ozone sensors.[51] For metal oxides, the grain size is usually tuned by calcination temperature. The increase in calcination temperature promotes the sintering of the metal oxide, leading to a large grain size. Nevertheless, the crystallinity also increases with rising calcination temperature. Katoch et al. also discussed the competitive effect between small grain size and high crystallinity.[48] In a CO sensor, when the ZnO grain size was below 50 nm, the sensing response did not improve with decreasing grain size because the crystallinity of ZnO calcined at low temperatures was poor. In our case, the sharp peaks in the XRD patterns of the five materials in Figure 1 all showed a highly crystalline phase of CuO. To synthesize CuO spheres in different sizes, 350 °C is the minimum temperature required for full conversion of malachite to CuO[52] so that 26 ± 4 nm is the smallest grain that we could reach by this approach. Although smaller metal oxide grains might possibly increase sensitivity further, they may be structurally less stable and exhibit an altered surface or different catalytic properties.

3.3.4. Influence of Electronic Properties of CuO Nanoparticles on Glucose Sensing. EIS data shed some additional light on the dependence of the glucose response slopes on CuO nanoparticle morphology and sensor electrode age. Several trends could be extracted from correlating response slopes to glucose (Table S1) with the charge transfer resistance associated with glucose oxidation or with the associated capacitances in equivalent circuit models. The data fell into two separate populations, the spherical CuO nanoparticles, which were single grains, and the platelets or needle-shaped CuO nanoparticles, which were polycrystalline. Figure S22 shows scatter plots containing all data for the spherical CuO-s

https://doi.org/10.1021/acsanm.2c05433
ACS Appl. Nano Mater. 2023, 6, 1475−1486

particles. The glucose calibration slope tended to decrease with higher charge transfer resistance, although several data points also fell below this trend line. The equivalent capacitance was a better predictor of the glucose calibration slope: as the capacitance increased, the slope increased, and capacitance values were lowest for the CuO-s particles with the largest grain size (CuO-s@500). The EIS data were also informative about the differences in the long-term stability of the different nanomaterials. Among the spherical morphologies, for CuO-s@500, which undergoes a large loss in sensitivity over several days, the total charge transfer resistance increases dramatically (by an order of magnitude) (Figure S23). At the same time, the capacitance decreases significantly (Figure S24). This may be explained by the formation of an increasingly thicker $Cu(OH)_2$ surface layer, which was identified by XPS (Figure S7), possibly due to incomplete regeneration of CuO by glucose with extended use. As the layer becomes thicker, it becomes more resistive and increases the separation between CuO cores in adjacent particles. It is also likely that this layer is poorly crystalline, resulting in a lower dielectric constant. All of these factors would lead to the lower capacitance that was observed. The patterns were different for the platelets and needle-shaped CuO particles (Figure S25). For CuO-p, while a higher charge transfer resistance was also associated with a lower response slope, the trend of increasing response slope with increasing capacitance values was less pronounced. For the needles, few changes in charge transfer resistance or capacitance were observed, consistent with the stability of the CuO-n electrodes with time. The greater long-term stability of CuO-n needles may be related to the fact that the nano-sized grains are part of larger particles, allowing grain boundaries to be protected from surface-layer degradation.

4. CONCLUSIONS

In this work, three different morphologies of copper oxide nanoparticles were synthesized. CuO spheres with various sizes were obtained by calcination of $Cu_2(OH)_2CO_3$ at different temperatures. CuO platelets were achieved by precipitating Cu^{2+} with OH^- at 70 °C. CuO needles were produced by precipitation of Cu^{2+} with hydroxide ions in the presence of CTAB and H_2O_2. We investigated how the synthesis influenced morphologies and explored how these morphologies affect the electrocatalytic oxidation of glucose. A detailed study was carried out to investigate the relationship between several properties of copper oxides, including the type of exposed crystal faces, specific surface areas with pore structure information, grain size, and electrocatalytic performance. Our results show that the electrocatalytic performance in glucose sensing correlates primarily with the grain size of copper oxide nanoparticles and the capacitance introduced therefrom. CuO nanoparticles with a small grain size of ~20 nm or smaller and a large number of grain boundaries can give high sensitivity over 2 $mA{\cdot}mM^{-1}{\cdot}cm^{-2}$. Specifically, CuO needles also have a wide linear range up to 5 mM and the best longer-term stability among the morphologies investigated here. Considering that blood glucose concentrations fall in the range of 3.5–5.5 mM, CuO nanoparticles with needle-like morphologies are potentially good candidates for glucose sensing applications (see also Table S2 for comparison with other systems).

By providing a correlation between the electrochemical performance and the morphology of nanoparticles, this work aims to achieve a more thorough understanding of CuO-based materials as electrocatalysts for commercialized biosensors. It may bring further insight into the primary contribution(s) of metal oxide-based materials in other applications and help design materials in the development of semiconductors, catalysts, and biomedical sensors. Future studies may include the design of a hierarchically structured material based on metal oxide nanoparticles with smaller sizes than those prepared in this study. A composite material (metal oxide/support) may also be of interest for future research because a support material can improve the stability of smaller metal oxide particles by preventing sintering or aggregation of the nanoparticles. Adjusting the ratio of metal oxide and support materials will also be considered to provide the best catalytic performance.

■ ASSOCIATED CONTENT

Supporting Information

The Supporting Information is available free of charge at https://pubs.acs.org/doi/10.1021/acsanm.2c05433.

XRD patterns, FT-IR spectra, XPS data, SEM images, TEM images, SAED patterns, nitrogen sorption isotherms, size histograms, amperometric responses, calculation details, EIS data, and glucose sensing data (PDF)

■ AUTHOR INFORMATION

Corresponding Author

Andreas Stein − *Department of Chemistry, University of Minnesota, Minneapolis, Minnesota 55455, United States;* orcid.org/0000-0001-8576-0727; Email: a-stein@umn.edu

Authors

Baoyue Fan − *Department of Chemistry, University of Minnesota, Minneapolis, Minnesota 55455, United States*

Brian D. Spindler − *Department of Chemistry, University of Minnesota, Minneapolis, Minnesota 55455, United States*

Wenyang Zhao − *Department of Chemistry, University of Minnesota, Minneapolis, Minnesota 55455, United States*

Hoffman Chan − *Department of Chemistry, University of Minnesota, Minneapolis, Minnesota 55455, United States*

Zhao Wang − *Department of Chemistry, University of Minnesota, Minneapolis, Minnesota 55455, United States*

Minog Kim − *Department of Chemistry, University of Minnesota, Minneapolis, Minnesota 55455, United States;* orcid.org/0000-0001-7963-1734

Yevedzo Chipangura − *Department of Chemistry, University of Minnesota, Minneapolis, Minnesota 55455, United States*

Philippe Bühlmann − *Department of Chemistry, University of Minnesota, Minneapolis, Minnesota 55455, United States;* orcid.org/0000-0001-9302-4674

Complete contact information is available at: https://pubs.acs.org/10.1021/acsanm.2c05433

Author Contributions

†B.F. and B.D.S. contributed equally to this manuscript. A.S. and B.F. conceived the project and designed the experiments. B.F. was responsible for material synthesis, data collection, visualization, and analysis. B.D.S. carried out EIS and other electrochemical analyses. W.Z. was responsible for collecting TEM images and SAED patterns. H.C. was responsible for parts of material synthesis. Z.W., M.K., and Y.C. collected SEM images. P.B. provided resources and feedback for electro-

https://doi.org/10.1021/acsanm.2c05433
ACS Appl. Nano Mater. 2023, 6, 1475−1486

chemical experiments. A.S., B.F., and B.D.S. wrote the manuscript. All authors contributed to the discussion and preparation of the manuscript and the Supporting Information.

Notes

The authors declare no competing financial interest.

■ ACKNOWLEDGMENTS

This work was partially supported by funding from the Industrial Partnership for Research in Interfacial and Materials Engineering (IPRIME-NMP) at the University of Minnesota. Parts of this work were carried out at the Characterization Facility, University of Minnesota, which receives partial support from the NSF through the MRSEC (Award Number DMR-2011401) and the NNCI (Award Number ECCS-2025124) programs. H.C. acknowledges a National Science Foundation (NSF) REU summer fellowship (Grant CHE-1851990). The authors thank Professor R.L. Penn for use of the powder X-ray diffractometer, Dr. Y. Sun for useful discussions and advice on schemes, and X. Dong for assistance with XPS analyses.

■ REFERENCES

(1) Lee, H.; Hong, Y. J.; Baik, S.; Hyeon, T.; Kim, D. H. Enzyme-Based Glucose Sensor: From Invasive to Wearable Device. *Adv. Healthcare Mater.* **2018**, *7*, No. 1701150.

(2) Dhara, K.; Mahapatra, D. R. Electrochemical Nonenzymatic Sensing of Glucose Using Advanced Nanomaterials. *Microchim. Acta* **2018**, *185*, No. 49.

(3) Hwang, D. W.; Lee, S.; Seo, M.; Chung, T. D. Recent Advances in Electrochemical Non-Enzymatic Glucose Sensors – A Review. *Anal. Chim. Acta* **2018**, *1033*, 1–34.

(4) Wang, J. Electrochemical Glucose Biosensors. *Chem. Rev.* **2008**, *108*, 814–825.

(5) Zhu, H.; LI, L.; Zhou, W.; Shao, Z.; Chen, X. Advances in Non-Enzymatic Glucose Sensors Based on Metal Oxides. *J. Mater. Chem. B* **2016**, *4*, 7333–7349.

(6) Yuan, J. H.; Wang, K.; Xia, X. Highly Ordered Platinum-Nanotubule Arrays for Amperometric Glucose Sensing. *Adv. Funct. Mater.* **2005**, *15*, 803–809.

(7) Ortega-Liebana, M. C.; Bonet-Aleta, J.; Hueso, J. L.; Santamaria, J. Gold-Based Nanoparticles on Amino-Functionalized Mesoporous Silica Supports as Nanozymes for Glucose Oxidation. *Catalysts* **2020**, *10*, No. 333.

(8) Wang, J.; Thomas, D. F.; Chen, A. Nonenzymatic Electrochemical Glucose Sensor Based on Nanoporous PtPb Networks. *Anal. Chem.* **2008**, *80*, 997–1004.

(9) Li, Y.; Deng, D.; Wang, H.; Huan, K.; Yan, X.; Luo, L. Controlled Synthesis of Cu-Sn Alloy Nanosheet Arrays on Carbon Fiber Paper for Self-Supported Nonenzymatic Glucose Sensing. *Anal. Chim. Acta* **2022**, *1190*, No. 339249.

(10) Morais, M.; Marques, A. C.; Ferreira, S. H.; Pinheiro, t.; Pimentel, A.; Macedo, P.; Martins, R.; Fortunato, E. Visible Photoluminescent Zinc Oxide Nanorods for Label-Free Non-enzymatic Glucose Detection. *ACS Appl. Nano Mater.* **2022**, *5*, 4386–4396.

(11) Tutel, Y.; Koylan, S.; Tunca, S.; Unalan, H. E. Nanometer-Thick Mn:NiO and Co:NiO Films for High Performance Non-enzymatic Biosensors. *ACS Appl. Nano Mater.* **2021**, *4*, 13871–13883.

(12) Huang, J.-F.; Zhu, Y.; Yang, X.; Chen, W.; Zhou, Y.; Li, C. Flexible 3D Porous CuO Nanowire Arrays for Enzymeless Glucose Sensing: In Situ Engineered versus Ex Situ Piled. *Nanoscale* **2015**, *7*, 559–569.

(13) Dai, Z.; Yang, A.; Bao, X.; Yang, R. Facile Non-Enzymatic Electrochemical Sensing for Glucose Based on Cu2O–BSA Nanoparticles Modified GCE. *Sensors* **2019**, *19*, 2824.

(14) Su, Y.; Luo, B.; Zhang, J. Z. Controllable Cobalt Oxide/Au Hierarchically Nanostructured Electrode for Nonenzymatic Glucose Sensing. *Anal. Chem.* **2016**, *88*, 1617–1624.

(15) Si, P.; Ding, S.; Yuan, J.; Lou, X. W.; Kim, D.-H. Hierarchically Structured One-Dimensional TiO2 for Protein Immobilization, Direct Electrochemistry, and Mediator-Free Glucose Sensing. *ACS Nano* **2011**, *5*, 7617–7626.

(16) Witkowska Nery, E.; Kundys, M.; Jeleń, P. S.; Jönsson-Niedziólka, M. Electrochemical Glucose Sensing: Is There Still Room for Improvement? *Anal. Chem.* **2016**, *88*, 11271–11282.

(17) Dong, Q.; Ryu, H.; Lei, Y. Metal Oxide Based Non-Enzymatic Electrochemical Sensors for Glucose Detection. *Electrochim. Acta* **2021**, *370*, No. 137744.

(18) Chitare, Y. M.; Jadhav, S. B.; Pawaskar, P. N.; Magdum, V. V.; Gunjakar, J. L.; Lokhande, C. D. Metal Oxide-Based Composites in Nonenzymatic Electrochemical Glucose Sensors. *Ind. Eng. Chem. Res.* **2021**, *60*, 18195–18217.

(19) Ashok, A.; Kumar, A.; Tarlochan, F. Highly Efficient Nonenzymatic Glucose Sensors Based on CuO Nanoparticles. *Appl. Surf. Sci.* **2019**, *481*, 712–722.

(20) Wang, B.; Wu, X. L.; Shu, C. Y.; Guo, Y. G.; Wang, C. R. Synthesis of CuO/Graphene Nanocomposite as a High-Performance Anode Material for Lithium-Ion Batteries. *J. Mater. Chem.* **2010**, *20*, 10661–10664.

(21) Zhu, G.; Xu, H.; Xiao, Y.; Liu, Y.; Yuan, A.; Shen, X. Facile Fabrication and Enhanced Sensing Properties of Hierarchically Porous CuO Architectures. *ACS Appl. Mater. Interfaces* **2012**, *4*, 744–751.

(22) Amaniampong, P. N.; Trinh, Q. T.; De Oliveira Vigier, K.; Dao, D. Q.; Tran, N. H.; Wang, Y.; Sherburne, M. P.; Jérôme, F. Synergistic Effect of High-Frequency Ultrasound with Cupric Oxide Catalyst Resulting in a Selectivity Switch in Glucose Oxidation under Argon. *J. Am. Chem. Soc.* **2019**, *141*, 14772–14779.

(23) Dubal, D. P.; Gund, G. S.; Lokhande, C. D.; Holze, R. CuO Cauliflowers for Supercapacitor Application: Novel Potentiodynamic Deposition. *Mater. Res. Bull.* **2013**, *48*, 923–928.

(24) Zhao, W.; Veerappan Vaithilingam, B.; Ghosh, S.; Li, X.; Geuzebroek, F.; El Nasr, A. S.; Khan, I.; Dara, S.; Mittal, N.; Daoutidis, P.; Al Hashimi, S.; Mkhoyan, K. A.; Al Wahedi, Y.; Tsapatsis, M.; Stein, A. High-Capacity Regenerable H_2S Sorbent for Reducing Sulfur Emissions. *Ind. Eng. Chem. Res.* **2021**, *60*, 14779–14787.

(25) Ahmad, R.; Vaseem, M.; Tripathy, N.; Hahn, Y. B. Wide Linear-Range Detecting Nonenzymatic Glucose Biosensor Based on CuO Nanoparticles Inkjet-Printed on Electrodes. *Anal. Chem.* **2013**, *85*, 10448–10454.

(26) Xu, W.; Dai, S.; Wang, X.; He, X.; Wang, M.; Xi, Y.; Hu, X. Nanorod-Aggregated Flower-Like CuO Grown on a Carbon Fiber Fabric for a Super High Sensitivity Non-Enzymatic Glucose Sensor. *J. Mater. Chem. B* **2015**, *3*, 5777–5785.

(27) Diao, K. K.; Xiao, Z.; Zhao, Y. Y. Specific Surface Areas of Porous Cu Manufactured by Lost Carbonate Sintering: Measurements by Quantitative Stereology and Cyclic Voltammetry. *Mater. Chem. Phys.* **2015**, *162*, 571–579.

(28) Reitz, E.; Jia, W.; Gentile, M.; Wang, Y.; Lei, Y. CuO Nanospheres Based Nonenzymatic Glucose Sensor. *Electroanalysis* **2008**, *20*, 2482–2486.

(29) Juska, V. B.; Pemble, M. E. A Critical Review of Electrochemical Glucose Sensing: Evolution of Biosensor Platforms Based on Advanced Nanosystems. *Sensors* **2020**, *20*, No. 6013.

(30) Sun, S.; Sun, Y.; Chen, A.; Zhang, X.; Yang, Z. Nanoporous Copper Oxide Ribbon Assembly of Free-Standing Nanoneedles as Biosensors for Glucose. *Analyst* **2015**, *140*, 5205–5215.

(31) Chen, C.; Qu, J.; Cao, C.; Niu, F.; Song, W. CuO Nanoclusters Coated with Mesoporous SiO_2 as Highly Active and Stable Catalysts for Olefin Epoxidation. *J. Mater. Chem.* **2011**, *21*, 5774–5779.

(32) Huang, F.; Zhong, Y.; Chen, J.; Li, S.; Li, Y.; Wang, F.; Feng, S. Nonenzymatic Glucose Sensor Based on Three Different CuO Nanomaterials. *Anal. Methods* **2013**, *5*, 3050–3055.

https://doi.org/10.1021/acsanm.2c05433
ACS Appl. Nano Mater. 2023, 6, 1475–1486

(33) Saraf, M.; Natarajan, K.; Mobin, S. M. Non-Enzymatic Amperometric Sensing of Glucose by Employing Sucrose Templated Microspheres of Copper Oxide (CuO). *Dalton Trans.* **2016**, *45*, 5833−5840.
(34) Velmurugan, M.; Karikalan, N.; Chen, S. M. Synthesis and Characterizations of Biscuit-like Copper Oxide for the Non-Enzymatic Glucose Sensor Applications. *J. Colloid Interface Sci.* **2017**, *493*, 349−355.
(35) Zhang, X.; Wang, G.; Liu, X.; Wu, J.; Li, M.; Gu, J.; Liu, H.; Fang, B. Different CuO Nanostructures: Synthesis, Characterization, and Applications for Glucose Sensors. *J. Phys. Chem. C* **2008**, *112*, 16845−16849.
(36) Liu, X.; Yang, Y.; Liu, R.; Shi, Z.; Ma, L.; Wei, M. Synthesis of Porous CuO Microspheres Assembled from (001) Facet-Exposed Nanocrystals with Excellent Glucose-Sensing Performance. *J. Alloys Compd.* **2017**, *718*, 304−310.
(37) Khairy, M.; Ismael, M. Remarkable Facets for Selective Monitoring of Biomolecules by Morphologically Tailored CuO Nanostructures. *J. Solid State Electrochem.* **2020**, *24*, 237−243.
(38) Pandey, P.; Packiyaraj, M. S.; Nigam, H.; Agarwal, G. S.; Singh, B.; Patra, M. K. Antimicrobial Properties of CuO Nanorods and Multi-Armed Nanoparticles against B. Anthracis Vegetative Cells and Endospores. *Beilstein J. Nanotechnol.* **2014**, *5*, 789−800.
(39) Cudennec, Y.; Lecerf, A.; Gérault, Y. Synthesis of $Cu(OH)_2$ and CuO by Soft Chemistry. *J. Solid State Inorg. Chem.* **1995**, *32*, 1013−1022.
(40) Yang, Y.; Xue, Y.; Cui, Z.; Zhao, M. Effect of Particle Size on Electrode Potential and Thermodynamics of Nanoparticles Electrode in Theory and Experiment. *Electrochim. Acta* **2014**, *136*, 565−571.
(41) Marioli, J. M.; Kuwana, T. Electrochemical Characterization of Carbohydrate Oxidation at Copper Electrodes. *Electrochim. Acta* **1992**, *37*, 1187−1197.
(42) Miller, B. Split-Ring Disk Study of the Anodic Processes at a Copper Electrode in Alkaline Solution. *J. Electrochem. Soc.* **1969**, *116*, 1675−1680.
(43) Zhao, J.; Wang, F.; Yu, J.; Hu, S. Electro-Oxidation of Glucose at Self-Assembled Monolayers Incorporated by Copper Particles. *Talanta* **2006**, *70*, 449−454.
(44) Prabhu, S. V.; Baldwin, R. P. Constant Potential Amperometric Detection of Carbohydrates at a Copper-Based Chemically Modified Electrode. *Anal. Chem.* **1989**, *61*, 852−856.
(45) Abd el Haleem, S. M.; Ateya, B. G. Cyclic Voltammetry of Copper in Sodium Hydroxide Solutions. *J. Electroanal. Chem. Interfacial Electrochem.* **1981**, *117*, 309−319.
(46) Sandford, C.; Edwards, M. A.; Klunder, K. J.; Hickey, D. P.; Li, M.; Barman, K.; Sigman, M. S.; White, H. S.; Minteer, S. D. A Synthetic Chemist's Guide to Electroanalytical Tools for Studying Reaction Mechanisms. *Chem. Sci.* **2019**, *10*, 6404−6422.
(47) Güemes, M.; Rahman, S. A.; Hussain, K. What Is a Normal Blood Glucose? *Arch. Dis. Child.* **2016**, *101*, 569−574.
(48) Katoch, A.; Sun, G. J.; Choi, S. W.; Byun, J. H.; Kim, S. S. Competitive Influence of Grain Size and Crystallinity on Gas Sensing Performances of ZnO Nanofibers. *Sens. Actuators, B* **2013**, *185*, 411−416.
(49) Bermejo-Deval, R.; Assary, R. S.; Nikolla, E.; Moliner, M.; Román-Leshkov, Y.; Hwang, S. J.; Palsdottir, A.; Silverman, D.; Lobo, R. F.; Curtiss, L. A.; Davis, M. E. Metalloenzyme-like Catalyzed Isomerizations of Sugars by Lewis Acid Zeolites. *Proc. Natl. Acad. Sci. U.S.A.* **2012**, *109*, 9727−9732.
(50) Katoch, A.; Abideen, Z. U.; Kim, H. W.; Kim, S. S. Grain-Size-Tuned Highly H_2-Selective Chemiresistive Sensors Based on ZnO-SnO2 Composite Nanofibers. *ACS Appl. Mater. Interfaces* **2016**, *8*, 2486−2494.
(51) Korotcenkov, G.; Han, S. D.; Cho, B. K.; Brinzari, V. Grain Size Effects in Sensor Response of Nanostructured SnO_2 and In_2O_3-Based Conductometric Thin Film Gas Sensor. *Crit. Rev. Solid State Mater. Sci.* **2009**, *34*, 1−17.
(52) Dörner, L.; Cancellieri, C.; Rheingans, B.; Walter, M.; Kägi, R.; Schmutz, P.; Kovalenko, M. V.; Jeurgens, L. P. H. Cost-Effective Sol-Gel Synthesis of Porous CuO Nanoparticle Aggregates with Tunable Specific Surface Area. *Sci. Rep.* **2019**, *9*, No. 11758.

https://doi.org/10.1021/acsanm.2c05433
ACS Appl. Nano Mater. 2023, 6, 1475−1486